Acta Pharmaceutica Sinica B 2024;14(5):2349−2357

Chinese Pharmaceutical Association
Institute of Materia Medica, Chinese Academy of Medical Sciences

Acta Pharmaceutica Sinica B

www.elsevier.com/locate/apsb
www.sciencedirect.com

SHORT COMMUNICATION

Development of an active-site titrant for SARS-CoV-2 main protease as an indispensable tool for evaluating enzyme kinetics

Rabea Voget[a], Julian Breidenbach[a,†], Tobias Claff[a,†], Alexandra Hingst[a,†], Katharina Sylvester[a], Christian Steinebach[a], Lan Phuong Vu[a], Renato H. Weiße[b], Ulrike Bartz[c], Norbert Sträter[b], Christa E. Müller[a], Michael Gütschow[a,*]

[a]*Pharmaceutical Institute, Pharmaceutical & Medicinal Chemistry, University of Bonn, Bonn 53121, Germany*
[b]*Institute of Bioanalytical Chemistry, Center for Biotechnology and Biomedicine, Leipzig University, Leipzig 04103, Germany*
[c]*Department of Natural Sciences, University of Applied Sciences Bonn-Rhein-Sieg, Rheinbach 53359, Germany*

Received 21 September 2023; received in revised form 25 January 2024; accepted 27 February 2024

KEY WORDS

COVID-19;
SARS-CoV-2;
Main protease;
Peptide nitriles;
Fluorogenic substrates;
Active-site titration;
X-ray crystallography;
Inner filter effect

Abstract A titrant for the SARS-CoV-2 main protease (M^{pro}) was developed that enables, for the first time, the exact determination of the concentration of the enzymatically active M^{pro} by active-site titration. The covalent binding mode of the tetrapeptidic titrant was elucidated by the determination of the crystal structure of the enzyme−titrant complex. Four fluorogenic substrates of M^{pro}, including a prototypical, internally quenched Dabcyl-EDANS peptide, were compared in terms of solubility under typical assay conditions. By exploiting the new titrant, key kinetic parameters for the M^{pro}-catalyzed cleavage of these substrates were determined.

© 2024 The Authors. Published by Elsevier B.V. on behalf of Chinese Pharmaceutical Association and Institute of Materia Medica, Chinese Academy of Medical Sciences. This is an open access article under the CC BY-NC-ND license (http://creativecommons.org/licenses/by-nc-nd/4.0/).

*Corresponding author.
E-mail address: guetschow@uni-bonn.de (Michael Gütschow).
†These authors made equal contributions to this work.

Peer review under the responsibility of Chinese Pharmaceutical Association and Institute of Materia Medica, Chinese Academy of Medical Sciences.

https://doi.org/10.1016/j.apsb.2024.03.001

2211-3835 © 2024 The Authors. Published by Elsevier B.V. on behalf of Chinese Pharmaceutical Association and Institute of Materia Medica, Chinese Academy of Medical Sciences. This is an open access article under the CC BY-NC-ND license (http://creativecommons.org/licenses/by-nc-nd/4.0/).

1. Introduction

The outbreak of the coronavirus disease (COVID-19) pandemic in 2019 led to a global health crisis of unprecedented proportions. COVID-19 is caused by the severe acute respiratory syndrome coronavirus 2 (SARS-CoV-2), an enveloped (+)-ss RNA virus with high similarities to other members of the betacoronavirus genus[1]. Once the spike protein has mediated host cell entry and endocytosis through receptor engagement[2], the viral genomic RNA is released into the cytoplasm and translated by the host cell machinery into two large polyproteins, pp1a and pp1ab, from which the main protease (M^{pro}) and the papain-like protease are excised. These enzymes process the viral polyproteins into non-structural proteins (nsps). The viral replication and transcription complex, composed of nsps, is required for the assembly of new virions, which are ultimately released from the host cell *via* exocytosis[3].

SARS-CoV-2 M^{pro} plays the predominant role in polyprotein processing that is indispensable for the viral life cycle. The enzyme is a homodimeric cysteine protease with each protomer consisting of three domains of which the chymotrypsin-like domains I and II form and enclose the M^{pro} substrate-binding site[4]. The catalytic dyad of each protomer comprises the residues Cys145 and His41, the latter facilitating deprotonation of the catalytic Cys145. The nucleophilic attack of the resulting thiolate on the carbonyl carbon of the scissile peptide bond initiates the acyl-transfer mechanism, leading to the release of the first product, while the N-terminal part of the substrate becomes covalently attached to the active site cysteine. Subsequent hydrolysis of the intermediate thioester generates the second product[4,5].

Its crucial role in SARS-CoV-2 replication, the low mutation rate of its binding domain as well as the lack of a homologous protease in humans renders M^{pro} a primary target for COVID-19 treatment[6-8]. Hence, M^{pro} inhibitors are constantly being developed and characterized as potential therapeutics[9-11], as well as activity-based probes[12-14].

The assessment of the inhibitory activity of such drug candidates is commonly based on biochemical assays to determine the kinetics of the M^{pro}-catalyzed conversion of artificial substrates. For comprehensive kinetic analyses, it is indispensable to know the exact molar concentration of enzyme active sites in a reaction mixture. Due to factors such as misfolding, inactivation, or self-degradation, a substantial fraction of the enzyme protein may be inactive. Active-site titration is the gold standard method to determine the active proportion of the total enzyme and to quantify the active enzyme concentration[15,16].

Our study aimed to introduce an active-site titrant for SARS-CoV-2 M^{pro}. Despite the overwhelming number of reports on M^{pro} inhibitors, such a tool compound is still lacking. We developed an aza-tetrapeptide derivative that is susceptible to being nucleophilically attacked by the active-site thiolate, resulting in an irreversible enzyme−titrant complex. Cocrystallization of the compound with M^{pro} conclusively showed its binding mode. By means of the new titrant, we determined the active-site concentration in M^{pro} samples and appraised the data for a comparative analysis of fluorogenic SARS-CoV-2 substrates.

2. Materials and methods

2.1. General biochemical settings

If not stated otherwise, all measurements were performed on a Fluostar Optima plate reader (BMG Labtech, Ortenberg, Germany) in black 96-well plates with a clear and flat bottom (Greiner Bio One, Kremsmünster, Austria). The assay buffer was 50 mmol/L 3-(*N*-morpholino)propanesulfonic acid (MOPS) buffer, pH 7.2, containing 10 mmol/L NaCl, 1 mmol/L EDTA and 0.01% (*v*/*v*) Triton X-100. M^{pro} was expressed with an N-terminal M^{pro} autocleavage site and a C-terminal His_{10} tag linked *via* an HRV 3C protease cleavage site. The C-terminally His-tagged M^{pro} was purified as previously described[17]. To obtain the native protease, the His tag was cleaved off using an HRV 3C protease as described[17]. The enzyme was stored in 50 mmol/L tris(hydroxymethyl)aminomethane (TRIS) buffer, pH 7.8, containing 100 mmol/L NaCl, 1 mmol/L ethylenediaminetetraacetic acid (EDTA) and 1 mmol/L dithiothreitol (DTT). M^{pro} batches were employed as solutions in concentrations ranging from 0.10 to 0.27 μg/μL (His-tagged protease) or as a 2.5 μg/μL solution (native M^{pro}), respectively. The substrate stock solutions were prepared in DMSO. The Dabcyl-EDANS substrate conversion was detected with an excitation filter of 340 nm and an emission filter of 490 nm; conversion of AMC substrates was detected at an excitation wavelength of 360 nm and an emission wavelength of 460 nm. The product formation was monitored at 37 °C. Data analysis was performed using Graph Pad Prism 8. The Dabcyl-EDANS substrate **5** (Dabcyl-Lys-Thr-Ser-Ala-Val-Leu-Gln-Ser-Gly-Phe-Arg-Lys-Met-Glu-EDANS) was purchased from Bachem (Bubendorf, Switzerland) and Merck (Darmstadt, Germany).

2.2. M^{pro} inactivation by the active-site titrant **1**

The second-order rate constant of inactivation, $k_{obs}/[I]$, was determined by means of a pre-incubation assay. In 21 μL of assay buffer, 2 μL of a 2.5 μmol/L solution of titrant **1** in DMSO was preincubated with 2 μL of a 0.11 μg/μL solution of His-tagged M^{pro} at 37 °C for three different time periods ranging from 30 to 60 s. Pre-incubation concentrations of M^{pro} and **1** were 8.8 ng/μL and 200 nmol/L, respectively. Two control reactions were performed, whereby 2 μL of DMSO was preincubated with 2 μL of the M^{pro} solution for 20 and 70 s. To start the reaction, 75 μL of a solution containing 73 μL of assay buffer and 2 μL of a substrate solution in DMSO (2.5 mmol/L in the case of substrate **2** and **5**, 10 mmol/L in the case of substrates **3** and **4**) was added and the reaction was monitored for 180 s. The final concentrations amounted to 50 nmol/L of **1**, 2.2 ng/μL of the enzyme, 50 μmol/L of substrate **2** or **5**, 200 μmol/L of substrate **3** or **4**, and 4% (*v*/*v*) of DMSO. The total volume per well was 100 μL. For each time of pre-incubation, initial velocities of product formation were determined by linear regression, related to the mean rate of the control reactions and plotted as residual initial rates against pre-incubation times (Supporting Information Fig. S1). The curve was analyzed by nonlinear regression using Eq. (1):

$$v_i = v_{i,0} \times e^{-k_{obs} \times t} \quad (1)$$

where v_i is the initial rate after pre-incubation with **1**, $v_{i,0}$ is the mean initial rate of the control, k_{obs} is the first-order rate constant of inactivation, and t is the incubation time. Dividing this value by

the pre-incubation concentration of **1** yielded $k_{obs}/[I]$, the second-order rate constant of inactivation. Due to limitations in the experimental setting with respect to shorter pre-incubation times, only a limit for $k_{obs}/[I]$ of >70,000 L/mol·s was obtained.

2.3. *Active-site titration of M^{pro}*

In order to evaluate the total concentration of active M^{pro} enzyme in the assay, product formation was monitored for mixtures of the substrate Boc-Abu-Tle-Leu-Gln-AMC (**2**) (unless noted otherwise) and C-terminally His-tagged or native M^{pro} which was preincubated with the titrant **1** (in at least 8 final concentrations ranging from 2 to 27.5 nmol/L) in assay buffer. Into a well containing 14 μL of assay buffer and 1 μL of the titrant solution in DMSO (or 1 μL of DMSO for the control, respectively), a volume of 10 μL of a mixture of enzyme solution (with the final protein concentration being noted for each experiment) and assay buffer was added. In order to achieve stoichiometric inactivation of the enzyme by the active-site titrant, incubation was performed for 5 min (unless noted otherwise) at 37 °C prior to starting the reaction by adding 25 μL of a mixture of 24 μL of assay buffer and 1 μL of substrate solution into the well. The final concentration of substrate **2** was 50 μmol/L and the final DMSO concentration was 4% (*v*/*v*). Product formation was monitored for 10 min and analyzed by linear regression. The product formation rate of the control without the titrant was set to 100%, to which the initial rates of the reactions with varying concentrations of titrant were related. The obtained values were plotted against the different titrant concentrations including the control. Linear regression of this plot provided an x-intercept which equals the active-site concentration of M^{pro}.

2.4. *Determination of K_m values*

Prior to K_m determinations, active-site titrations of the corresponding His-tagged or native M^{pro} batches were performed and the active-site M^{pro} concentration was adjusted. Initial velocities of substrate conversion by M^{pro} were determined at 13 or 15 different substrate concentrations ranging from 2.5 to 100 μmol/L or 2.5−125 μmol/L for **2**, at 16 different substrate concentrations of 2.5−200 μmol/L for **5**, and at 20 different concentrations between 0.1 and 10 mmol/L for **3** and **4**. A volume of 2.5 μL of the substrate solution was added to 22.5 μL of assay buffer in each well. The reaction was started by adding 25 μL of a mixture of the enzyme solution and assay buffer and monitored at 37 °C. The total volume in each well was 50 μL and the final DMSO concentration was 5% (*v*/*v*). The final concentration of active enzyme was 33 nmol/L. Initial velocities were determined by linear regression of the first 10 min for each substrate concentration. K_m and V_{max} for **2** and **5** were determined by fitting the data to the Michaelis−Menten equation. V_{max}^{app} values for **3** and **4** were obtained by means of a fourth-order polynomial equation.

2.5. *Translation of fluorescence into product concentrations and determination of k_{cat} values*

2.5.1. *Boc-Abu-Tle-Leu-Gln-AMC (**2**) and Dabcyl-Lys-Thr-Ser-Ala-Val-Leu-Gln-Ser-Gly-Phe-Arg-Lys-Met-Glu-EDANS (**5**)*

Inner filter effect (IFE) corrections were applied for each concentration employed in the K_m determination of **2** and **5**. The correction factors (f) were determined as follows. To 47.5 μL of assay buffer, 2.5 μL of a solution of **2** or **5** was added. The final substrate concentrations were either zero or corresponded to those from the K_m determinations and the final DMSO concentration was 5% (*v*/*v*). Fluorescence intensity was monitored for 5 min prior to the addition of 1 μL of a 51 μmol/L solution of free AMC (for **2**) or free EDANS (for **5**) (final concentration: 1 μmol/L each) and further monitoring for 5 min. Mean fluorescence (F) was calculated for each sample with and without the free fluorophore. The correction factors were determined as Eq. (2):

$$f = \left(F_{\text{substrate+fluorophore}} - F_{\text{substrate}}\right) \,/\, \left(F_{\text{control+fluorophore}} - F_{\text{control}}\right) \tag{2}$$

The corrected fluorescence (F_{corr}) for the K_m determination was calculated as Eq. (3):

$$F_{corr} = F_{obs} \,/\, f \tag{3}$$

with F_{obs} being the observed fluorescence (Supporting Information Fig. S4).

Calibration of fluorescence readout *versus* concentration of free AMC (for **2**) or EDANS (for **5**) was employed to allow for the translation of F_{corr} into product concentrations. To do so, 47.5 μL of assay buffer was supplemented with 2.5 μL of the respective fluorophore solution (or only DMSO), yielding final concentrations of 0−1000 nmol/L (AMC) or 0−10 μmol/L (EDANS), respectively. Fluorescence intensity was monitored for 5 min and mean values were calculated for each sample. ΔFU was defined as the difference of the fluorescence signal in the presence of the fluorophore at given concentration from the value at [fluorophore] = 0. The calibration lines of ΔFU *versus* [AMC] and ΔFU *versus* [EDANS] were applied for the determination of the product formation rate of **2** and **5** (Supporting Information Fig. S7).

2.5.2. *Ac-Abu-Orn-Leu-Gln-AMC (**3**) and Succinyl-Abu-Tle-Leu-Gln-AMC (**4**)*

For each substrate, calibration was performed on the basis of nine different concentrations of AMC in the presence of the respective substrate in a constant concentration equaling the substrate peak concentration $[S]_p$. To 49 μL of a solution consisting of 47.5 μL assay buffer and 1.5 μL substrate in DMSO, 1 μL of an AMC solution in DMSO (or only DMSO) was added. The final concentrations were 3.48 mmol/L of **3**, 3.30 mmol/L of **4**, 0−15 μmol/L of AMC and 5% (*v*/*v*) of DMSO. Fluorescence intensity was monitored for 1 min and mean values were calculated for each sample. ΔFU was defined as the difference of the fluorescence signal in the presence of AMC at given concentration from the value at [AMC] = 0. Calibration lines of ΔFU *versus* [AMC] were generated for **3** and **4** separately (Supporting Information Fig. S7) and applied for the translation of the maximum initial fluorescence formation rate into a maximum initial product formation rate at the substrate peak concentration $[S]_p$.

2.6. *Determination of substrate solubility, X-ray crystallography, synthetic chemistry*

The corresponding material can be found in the Supporting Information.

3. Results and discussion

In search of an active-site titrant for M^{pro}, we considered several chemotypes of covalent M^{pro} inhibitors, including peptide nitriles[18], of which the representative nirmatrelvir has already

gained market approval as an oral medication with substantial clinical efficacy[19,20]. Nirmatrelvir acts as an active-site directed, covalent drug, with M^{pro} inhibition being time-dependent and reversible[21-23]. For the design of an active-site titrant, the azanitrile structure was chosen, known to provoke a blockade of the active-site cysteine residue of human and schistosomal cysteine proteases due to the formation of a highly stabilized isothiosemicarbazide adduct[24,25]. Towards SARS-CoV-2 M^{pro}, such agents exhibited an irreversible mode of action[17]. The peptidomimetic structure of the envisaged titrant **1** (Scheme 1) comprised aza-phenylalanine-nitrile at P1, and phenylalanine, *tert*-leucine and 2-aminobutyric acid at P2−P4 positions. The synthetic route included the preparation of the hydrazide **6**, which, after separation from the terminally methylated isomer, was condensed with benzaldehyde to yield **7**. The subsequently applied conditions led to the hydrogenolytic Cbz-deprotection and the concomitant reduction of the hydrazone moiety. The resulting hydrazide functionality was not affected in the following steps of extending the peptide by two amino acids. Intermediate **9** was subjected to an electrophilic cyanation yielding azanitrile **1**. Compound **1** showed pronounced and time-dependent inhibition of M^{pro} and the fast enzyme inactivation was reflected by a second-order rate constant of >70,000 L/mol·s (Supporting Information Fig. S1).

To understand the binding mode of titrant **1** to M^{pro} in detail, we used X-ray crystallography to acquire a complex structure at a resolution of 1.77 Å (Fig. 1). Two protein chains are present in the asymmetric unit. In chain A, the titrant has higher B-factors and the electron density is not as well defined as in chain B (Supporting Information Fig. S10A), in which the ligand is involved in crystal packing interactions (see Supporting Information, X-ray crystallography section, for further details). The sulfur of the active site Cys145 and the cyano carbon of the warhead were covalently bonded generating an −N(Me)−N(Bn)−C(=NH)−S− linkage between the titrant and the target protease. The thioimidate nitrogen occupied the oxyanion hole and formed a hydrogen bond with the backbone NH of Cys145. The aromatic ring of the P1 building block did not penetrate deeply into the S1 pocket and was located above the S1 amino acid Glu166[26-28] and established hydrophobic contacts with Asn142 including a π-stacking interaction with the Leu141−Asn142 peptide bond. The P1 phenyl ring and residue Asn142 had weaker density and elevated B-factors indicating flexibility. The side chain of P2

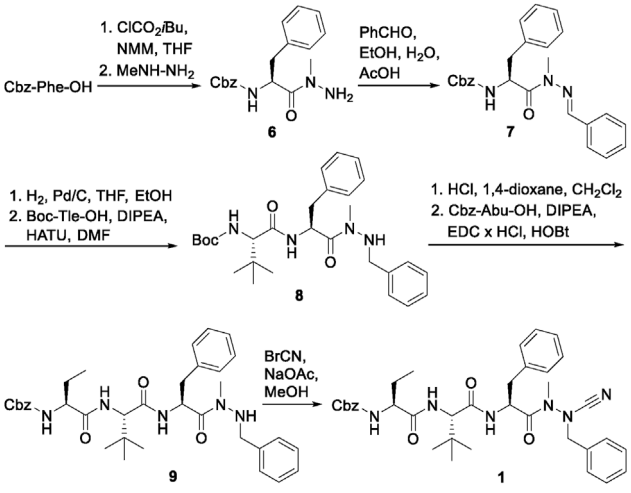

Scheme 1 Synthesis of the active-site titrant **1**.

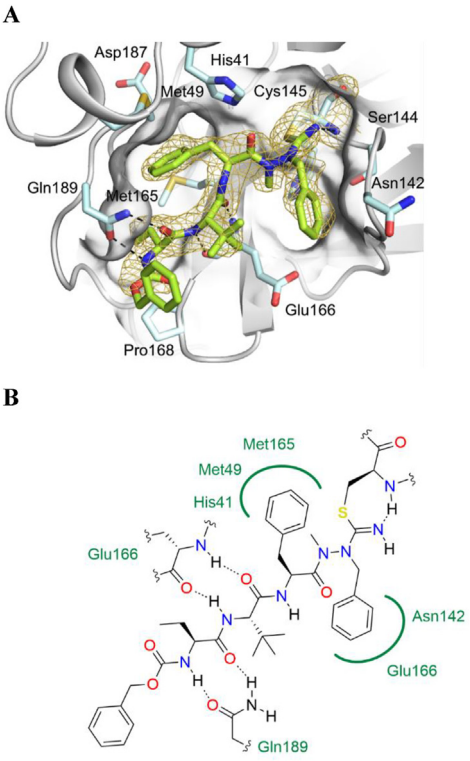

Figure 1 Co-crystal structure of **1** with SARS-CoV-2 M^{pro} (PDB ID: 8QDC, chain A). (A) Covalent binding of **1** to the M^{pro} active site and accessible subsites. The $(2F_o-F_c)$-type electron density of the ligand and Cys145 is shown as yellow mesh (contoured at 1 σ). (B) 2D interaction diagram of **1** with M^{pro}.

phenylalanine was accommodated in the hydrophobic S2 pocket formed by Met49, Met165, and His41. Glu166 was involved in backbone−backbone hydrogen bonding interactions with **1**. The carboxamide group of Gln189 formed hydrogen bonds to the NH and CO groups of aminobutyric acid at P4 position. An involvement of Gln189 in such a hydrogen bond network has so far rarely been observed in M^{pro}−inhibitor complexes[9]. The terminal benzyl group exhibited significant flexibility in chain A as indicated by the lack of electron density (Fig. 1A). Its conformation was modeled according to the well-defined density in chain B. To further characterize the binding mode of **1** in the active site of M^{pro}, we compared it with the complex of a peptidic substrate and M^{pro} whose catalytic Cys145 was mutated to Ala (Fig. S10B)[26]. The superposition of both complexes showed significant rearrangements of the loops with the residues Met49, Asn142, and Gln189 which leads to the required binding pocket expansion to accommodate **1**. Overall, the crystallographically confirmed covalent binding mode and the fast and irreversible inhibition characteristics suggested **1** to react with the active site in a 1:1 stoichiometry and to therefore constitute an appropriate probe for active-site titration of M^{pro}.

Since our titrant exhibited a very high second-order rate constant of inactivation, we were able to follow recommendations for an accurate active-site titration[15,16], *i.e.*, a final titrant concentration not exceeding 50 nmol/L and representing up to 0.7 equivalents. In our typical setting, a sufficient pre-incubation time of 5 min was chosen and a 7-amino-4-methyl-coumarin (AMC)-based substrate (**2**, for the structure see Supporting Information Fig. S8) was used for the subsequent reaction. An exemplary

experiment to determine the molar active-site concentration of the enzyme, $[E]_0$, is depicted in Fig. 2. The results were reproducible when varying the pre-incubation time (Supporting Information Fig. S2) or employing substrates other than **2** (Supporting Information Fig. S3). For the calculation of the proportion of active enzyme, a mass of 34.21 kDa per monomer was assumed[5].

The quantification of the active enzyme is a fundamental prerequisite for analyzing enzyme-catalyzed reactions and enzyme−inhibitor interactions while abiding by the principles of Michaelis−Menten kinetics. Hence, as a first application of our titrant, it was employed to characterize the four fluorogenic M^{pro} substrates **2**−**5** (Table 1, Supporting Information Fig. S8). The AMC-based substrate **2** has already proven to be suitable for the kinetic investigation of potential M^{pro} inhibitors[17]. Substrates **3** and **4** constitute more polar derivatives of **2**, which were newly prepared (Supporting Information Scheme S1) in order to improve their solubility, thus making the substrates applicable at higher concentrations and beneficial for the examination of particularly potent inhibitors. Substrate **5** is a commercially available and commonly employed, internally quenched fluorogenic substrate[29,30]. Its structure comprises the quencher 4-((4-(dimethylamino)phenyl)azo)benzoic acid (Dabcyl) and the fluorescent donor 5-((2-aminoethyl)amino)naphthalene-1-sulfonic acid (EDANS) on opposite sides of the Gln−Ser scissile bond.

Initially, to determine key kinetic parameters, concentration-dependent measurements of the cleavage of the fluorogenic substrate **2** catalyzed by either the C-terminally His-tagged M^{pro} or the native M^{pro} were performed. We considered the influence of the inner filter effect (IFE)[31], a phenomenon resulting in an attenuation of the ratio of fluorescence signal to the concentration of the fluorescent cleavage product due to absorbance of the emitted light by the substrate (Supporting Information Fig. S4). The comparison of the catalytic efficiency of both constructs necessitated the knowledge of the active site concentrations, determined by means of the titrant **1** (Fig. 2, Supporting Information Fig. S5). In our experiment, a higher fraction of the active enzyme, relative to the total protein content, was observed for the His-tagged M^{pro} (56%) than for the native M^{pro} (20%). We obtained k_{cat}/K_m values of 2170 L/mol·s for the native M^{pro} and of 2030 L/mol·s for the C-terminally His-tagged M^{pro} (Fig. 3A, Supporting Information Fig. S6). It has been reported that a His tag at the C-terminus of M^{pro} has a less

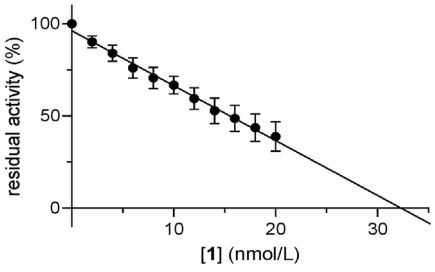

Figure 2 Active-site titration of His-tagged SARS-CoV-2 M^{pro} (2.0 ng/μL) with **1** under use of substrate **2** (50 μmol/L). The data are means from five independent experiments performed with aliquots from the same enzyme preparation. The equivalent point, obtained by linear regression as the *x*-axis intercept, corresponded to an active enzyme concentration of 32.6 ± 3.8 nmol/L and a proportion of 56% active enzyme. The standard deviations refer to the linear regression.

Table 1 Kinetic and physicochemical parameters of fluorogenic M^{pro} substrates **2**−**5**.

	Substrate	k_{cat} (s^{-1})	k_{cat}/K_m (L/mol·s)	K_m ± SE[a] (μmol/L)	k_{cat}^{app}[b] (s^{-1})	k_{2nd}^{app}[c] (L/mol·s)	Solubility ± SD[d] (μmol/L)
2	Boc-Abu-Tle-Leu-Gln-AMC	0.173	2030	85.2 ± 5.6	N.A.[e]	N.A.	19.3 ± 2.6
3	Ac-Abu-Orn-Leu-Gln-AMC	N.A.	N.A.	N.A.	0.14	175	5480 ± 720
4	Succinyl-Abu-Tle-Leu-Gln-AMC	N.A.	N.A.	N.A.	0.43	567	6210 ± 180
5	Dabcyl-Lys-Thr-Ser-Ala-Val-Leu-Gln-Ser-Gly-Phe-Arg-Lys-Met-Glu-EDANS	2.14	8200	261 ± 19	N.A.	N.A.	47.4 ± 1.3

[a]Standard errors refer to the non-linear regression.
[b]Apparent k_{cat} value, refers to the rate at the peak obtained with a substrate concentration $[S]_p$[39].
[c]Apparent second-order rate constant, the quotient of the apparent k_{cat} value and the substrate concentration at $k_{cat}^{app}/2$.
[d]HPLC-based determination of the solubility under assay conditions, *i.e.*, 50 mmol/L 3-(*N*-morpholino)propanesulfonic acid (MOPS) buffer, pH 7.2, 10 mmol/L NaCl, 1 mmol/L EDTA, 0.01% (*v*/*v*) Triton X-100, 5% (*v*/*v*) DMSO, 37 °C.
[e]N.A. not applicable.

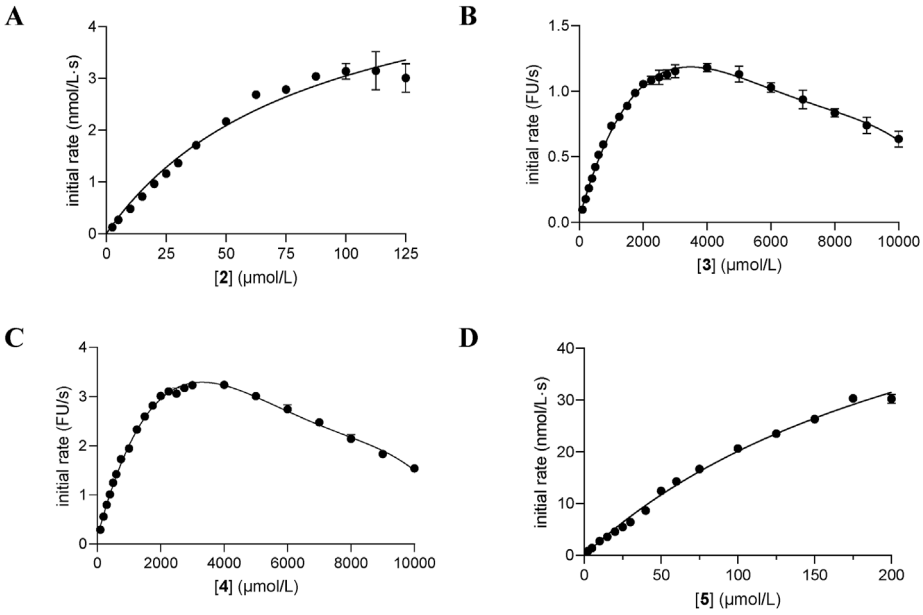

Figure 3 Determination of kinetic parameters for conversion of substrates **2**–**5** by His-tagged SARS-CoV-2 M^{pro}. Data are means of triplicate measurements. (A, D) IFE-corrected fluorescence was translated into product concentration. (B, C) IFE correction was not implemented. (A) Determination of k_{cat}, k_{cat}/K_m, and K_m values of substrate **2**. (B) Determination of the k_{cat}^{app} value of substrate **3**. (C) Determination of the k_{cat}^{app} value of substrate **4**. (D) Determination of k_{cat}, k_{cat}/K_m, and K_m values of substrate **5**.

pronounced effect on the specific activity, whereas an N-terminal His tag was detrimental to its activity[32,33].

Next, kinetic parameters of the His-tagged M^{pro}-catalyzed cleavage of the substrates **2**–**5** were determined and compared. Substrate consumption was observed by means of fluorescence emitted by the cleavage product AMC in case of substrates **2**, **3**, and **4**, and by the EDANS-containing peptide portion in case of **5**, respectively. The Michaelis–Menten curves of **2** (Fig. 3A) and **5** (Fig. 3D) yielded V_{max} and K_m values, the latter were similar to literature data for substrate **2**, used under somewhat different conditions[17], and for **5**[34,35]. Our data were also in the same order of magnitude as those reported for closely related Dabcyl-EDANS substrates (Dabcyl-Lys-Thr-Ser-Ala-Val-Leu-Gln-Ser-Gly-Phe-Arg-Lys-Met-Glu(EDANS)-OH, Dabcyl-Lys-Thr-Ser-Ala-Val-Leu-Gln-Ser-Gly-Phe-Arg-Lys-Met-Glu(EDANS)-NH_2)[36-38].

Substrates **3** and **4** displayed decreasing initial velocities at high substrate concentrations (Fig. 3B and C). Apart from the IFE, a common cause for the observed phenomenon, substrate inhibition might be another confounder contributing to the seemingly decreasing product formation rates. It occurs in approximately 20% of all studied enzymes, has diverse biological functions and is especially probable at high substrate concentrations[39,40]. Owing to this non-conforming Michaelis–Menten appearance, curves of **3** and **4** were analyzed by means of a fourth-order polynomial equation. An apparent maximum velocity V_{max}^{app} was determined as the rate corresponding to the substrate peak concentration $[S]_p$, which relates to the optimum of the respective curve. $[S]_p$ values of **3** and **4** were 3.48 and 3.30 mmol/L, respectively.

In order to calculate the turnover number k_{cat}, the true kinetic parameter, we applied Eq. (4):

$$k_{cat} = V_{max}/[E]_0 \quad (4)$$

The active-site concentration $[E]_0$ was accessible with the help of our titration reagent **1** (Fig. 2). Since product formation was initially quantified by means of the fluorescence signal, V_{max} was obtained in fluorescence units per time, which required the translation of the numerator into corresponding product concentrations. To allow for this conversion while taking a possible IFE into account, we performed different types of calibrations.

For substrates **2** and **5**, fluorescence values at each concentration were corrected by the IFE by means of experimentally determined correction factors[4,41]. While only a slight effect was observed for **2** within the concentration range up to 150 µmol/L, substrate **5** exhibited a pronounced IFE (Supporting Information Fig. S4). Calibration lines of fluorescence *versus* concentration of the free fluorophore AMC (**2**) or EDANS (**5**) were applied for the translation of the corrected fluorescence into product concentrations (Supporting Information Fig. S7A and S7D).

In case of substrates **3** and **4**, the IFE was considered only for the substrate concentration $[S]_p$ that caused the highest fluorescence readout per time (Fig. S7B, S7C). The apparent turnover numbers were calculated using Eq. (5):

$$k_{cat}^{app} = V_{max}^{app}/[E]_0 \quad (5)$$

and are listed in Table 1. K_m values were not accessible for both substrates.

In addition to the kinetic examination, an HPLC-based determination of the solubility of the four substrates under assay conditions, in the absence of M^{pro}, was performed (Table 1; Supporting Information Fig. S9). We applied a thermodynamic shake-flask solubility method to quantify the saturation concentration of the compounds in equilibrium with an excess of undissolved solid[42]. As expected, the solubility of **3** and **4** was improved in comparison to the parent compound **2**; the introduction of additional solubilizing groups led to a 250-fold increase. The Dabcyl-EDANS substrate **5** exhibited a 2.5-fold higher solubility than **2**. It should be noted, however, that biochemical M^{pro} assays occur under conditions of kinetic solubility of the substrates, which may attain a high degree of supersaturation,

supported by solute−solute interactions between substrate and enzyme[43]. Since the kinetic solubility is typically higher than the thermodynamic solubility, the application of substrates in concentrations exceeding their thermodynamic solubility limits is acceptable in enzyme assays[43,44]. Solubility properties are relevant for kinetic investigation since they define the maximum substrate concentration in biochemical assays which, in turn, affects the competition of substrate and inhibitor for the active site.

With the kinetic data for **2**−**5** in hand, obtained by applying the active-site titrant **1**, and under consideration of the physicochemical parameters, the four substrates were compared (Table 1). While **2** and **5** displayed moderate, double-digit micromolar K_m values, the latter had the better k_{cat}/K_m value, the decisive kinetic parameter. Hence, the difference is driven by the higher turnover rate that governs the M^{pro}-catalyzed conversion of substrate **5**. This finding might indicate that favorable interactions of the C-terminal heptapeptide of **5** with the primed subsites of M^{pro} facilitate the rate-limiting formation of the acyl-enzyme intermediate. Both substrates, **2** and **5**, are poorly soluble, prohibiting their application in higher concentrations. The apparent first-order rate constants k_{cat}^{app} of **3** and **4** are similar to the k_{cat} value of **2**. In comparison to **5**, the presence of the coumarin in substrates **2**−**4** might exert a detrimental effect on the turnover rate. Substrates **3** and **4** allow for a fast conversion and, thus, an adequate readout, only when employed in millimolar concentrations. This, however, is possible because the newly synthesized substrates **3** and **4** exhibit remarkable solubility in accordance with their polar molecular structure. The apparent second-order rate constants of **3** and **4** are comparably low (175 and 567 L/mol·s *versus* k_{cat}/K_m of 2030 and 8200 L/mol·s, Table 1). This poor kinetic performance, as well as the absence of precise K_m values assigned to these two substrates, make them less attractive for the application in M^{pro} assays. The k_{cat}/K_m value of the Dabcyl-EDANS substrate **5** exceeds the specificity constants of the other substrates, indicating it to be particularly suited for monitoring the proteolytic activity of M^{pro}. However, a practical disadvantage encountered with **5** is the lower fluorescence yield, compared to **2**−**4**, resulting from the same amount of cleavage product.

4. Conclusions

We have designed, synthesized and applied an aza-tetrapeptide nitrile as an active-site titrant for M^{pro}. Its binding mode was elucidated by means of the X-ray crystal structure of the enzyme complexed with the titrant at high resolution. We exploited the newly gained knowledge of the protease's active-site concentration to comprehensively characterize four fluorogenic substrates (**2**−**5**) regarding their kinetic properties. For the commercially available substrate **5**, a k_{cat}/K_m value of 8200 L/mol·s was determined. This is a result of general interest, since this prototypical, internally quenched fluorogenic substrate is frequently used in medicinal chemistry approaches towards SARS-CoV-2.

The titrant **1** could prove valuable for applications beyond those presented in this work. As the potency of newly developed M^{pro} inhibitors continues to improve[8,20,45-47], making them applicable in low nanomolar concentrations, a sufficient excess of inhibitor over enzyme needs to be secured *via* active-site titration, in order to determine kinetic parameters under Michaelis−Menten conditions. When evaluating tight-binding M^{pro} inhibitors, K_i values are regularly calculated by means of the Morrison equation under consideration of the total enzyme concentration[28,48,49], where the exact determination of $[E]_0$ by employing a titration reagent allows for higher accuracy of the calculated kinetic parameters.

Moreover, artificial substrates with poor kinetic performance, *i.e.,* low turnover numbers, require relatively high enzyme concentrations to generate a sufficient analytical readout, which, in turn, may counteract the stoichiometric surplus of the inhibitor. Such a scenario is common in the course of M^{pro} inhibitor development and necessitates the precise determination of the active-site concentration by titration. The active-site titrant **1** introduced in this study is therefore expected to serve as a valuable tool compound for anti-SARS-CoV-2 drug discovery.

Acknowledgments

The authors acknowledge support by Dr. Carina Lemke and Marion Schneider. Christa E. Müller and Michael Gütschow were supported by the Volkswagen Foundation (9A894), Rabea Voget, Christian Steinebach, Christa E. Müller and Michael Gütschow by the German Research Foundation (RTG 2873) and Norbert Sträter by the Volkswagen Foundation (9A850). We acknowledge DESY (Hamburg, Germany), a member of the Helmholtz Association HGF, and the EMBL for the provision of experimental facilities at synchrotron beamlines P13 and P14 and the MX Laboratory at the Helmholtz Zentrum Berlin (BESSY II) for beam time. We would like to thank Selina Storm for assistance in using the EMBL beamlines.

Author contributions

Michael Gütschow designed the study. Rabea Voget, Julian Breidenbach, Tobias Claff, Alexandra Hingst, Katharina Sylvester and Renato H. Weiβe performed experiments. All authors analyzed data. Norbert Sträter, Christa E. Müller and Michael Gütschow supervised the project. Rabea Voget and Michael Gütschow wrote the manuscript with contributions from all co-authors.

Conflicts of interest

The authors declare no conflicts of interest.

Appendix A. Supporting information

Supporting information to this article can be found online at https://doi.org/10.1016/j.apsb.2024.03.001.

References

1. Lu R, Zhao X, Li J, Niu P, Yang B, Wu H, et al. Genomic characterisation and epidemiology of 2019 novel coronavirus: implications for virus origins and receptor binding. *Lancet* 2020;**395**:565−74.
2. Hoffmann M, Kleine-Weber H, Schroeder S, Krüger N, Herrler T, Erichsen S, et al. SARS-CoV-2 cell entry depends on ACE2 and TMPRSS2 and is blocked by a clinically proven protease inhibitor. *Cell* 2020;**181**:271−80.
3. V'kovski P, Kratzel A, Steiner S, Stalder H, Thiel V. Coronavirus biology and replication: implications for SARS-CoV-2. *Nat Rev Microbiol* 2021;**19**:155−70.
4. Zhang L, Lin D, Sun X, Curth U, Drosten C, Sauerhering L, et al. Crystal structure of SARS-CoV-2 main protease provides a basis for

design of improved α-ketoamide inhibitors. *Science* 2020;**368**:409−12.
5. Hu Q, Xiong Y, Zhu GH, Zhang YN, Zhang YW, Huang P, et al. The SARS-CoV-2 main protease (M^{pro}): structure, function, and emerging therapies for COVID-19. *MedComm* 2022;**3**:e151.
6. Gil C, Ginex T, Maestro I, Nozal V, Barrado-Gil L, Cuesta-Geijo MÁ, et al. COVID-19: drug targets and potential treatments. *J Med Chem* 2020;**63**:12359−86.
7. Gao S, Huang T, Song L, Xu S, Cheng Y, Cherukupalli S, et al. Medicinal chemistry strategies towards the development of effective SARS-CoV-2 inhibitors. *Acta Pharm Sin B* 2022;**12**:581−99.
8. Li G, Hilgenfeld R, Whitley R, De Clercq E. Therapeutic strategies for COVID-19: progress and lessons learned. *Nat Rev Drug Discov* 2023;**22**:449−75.
9. Gao K, Wang R, Chen J, Tepe JJ, Huang F, Wei GW. Perspectives on SARS-CoV-2 main protease inhibitors. *J Med Chem* 2021;**64**:16922−55.
10. La Monica G, Bono A, Lauria A, Martorana A. Targeting SARS-CoV-2 main protease for treatment of COVID-19: covalent inhibitors structure−activity relationship insights and evolution perspectives. *J Med Chem* 2022;**65**:12500−34.
11. Ding D, Xu S, da Silva-Júnior EF, Liu X, Zhan P. Medicinal chemistry insights into antiviral peptidomimetics. *Drug Discov Today* 2023;**28**:103468.
12. van de Plassche MAT, Barniol-Xicota M, Verhelst SHL. Peptidyl acyloxymethyl ketones as activity-based probes for the main protease of SARS-CoV-2. *Chembiochem* 2020;**21**:3383−8.
13. Cheng Y, Borum RM, Clark AE, Jin Z, Moore C, Fajtová P, et al. A dual-color fluorescent probe allows simultaneous imaging of main and papain-like proteases of SARS-CoV-2-infected cells for accurate detection and rapid inhibitor screening. *Angew Chem Int Ed* 2022;**61**:e202113617.
14. Vanhoutte R, Barniol-Xicota M, Chiu W, Vangeel L, Jochmans D, De Jonghe S, et al. Azapeptide activity-based probes for the SARS-CoV-2 main protease enable visualization of inhibition in infected cells. *Chem Sci* 2023;**14**:1666−72.
15. Knight CG. Active-site titration of peptidases. *Methods Enzymol* 1995;**248**:85−101.
16. Zhang R, Wong K. High performance enzyme kinetics of turnover, activation and inhibition for translational drug discovery. *Expet Opin Drug Discov* 2017;**12**:17−37.
17. Breidenbach J, Lemke C, Pillaiyar T, Schäkel L, Al Hamwi G, Diett M, et al. Targeting the main protease of SARS-CoV-2: from the establishment of high throughput screening to the design of tailored inhibitors. *Angew Chem Int Ed* 2021;**60**:10423−9.
18. Frizler M, Stirnberg M, Sisay MT, Gütschow M. Development of nitrile-based peptidic inhibitors of cysteine cathepsins. *Curr Top Med Chem* 2010;**10**:294−322.
19. Focosi D, McConnell S, Shoham S, Casadevall A, Maggi F, Antonelli G. Nirmatrelvir and COVID-19: development, pharmacokinetics, clinical efficacy, resistance, relapse, and pharmacoeconomics. *Int J Antimicrob Agents* 2023;**61**:106708.
20. Zhu KW. Deuremidevir and simnotrelvir-ritonavir for the treatment of COVID-19. *ACS Pharmacol Transl Sci* 2023;**6**:1306−9.
21. Owen DR, Allerton CM, Anderson AS, Aschenbrenner L, Avery M, Berritt S, et al. An oral SARS-CoV-2 Mpro inhibitor clinical candidate for the treatment of COVID-19. *Science* 2021;**374**:1586−93.
22. Algar-Lizana S, Bonache MÁ, González-Muñiz R. SARS-CoV-2 main protease inhibitors: what is moving in the field of peptides and peptidomimetics?. *J Pept Sci* 2023;**29**:e3467.
23. Duan Y, Zhou H, Liu X, Iketani S, Lin M, Zhang X, et al. Molecular mechanisms of SARS-CoV-2 resistance to nirmatrelvir. *Nature* 2023;**622**:376−82.
24. Löser R, Frizler M, Schilling K, Gütschow M. Azadipeptide nitriles: highly potent and proteolytically stable inhibitors of papain-like cysteine proteases. *Angew Chem Int Ed* 2008;**47**:4331−4.
25. Jílková A, Horn M, Fanfrlík J, Küppers J, Pachl P, Řezáčová P, et al. Azanitrile inhibitors of the SmCB1 protease target are lethal to *Schistosoma mansoni*: structural and mechanistic insights into chemotype reactivity. *ACS Infect Dis* 2021;**7**:189−201.
26. Shaqra AM, Zvornicanin SN, Huang QJ, Lockbaum GJ, Knapp M, Tandeske L, et al. Defining the substrate envelope of SARS-CoV-2 main protease to predict and avoid drug resistance. *Nat Commun* 2022;**13**:3556.
27. Lin M, Zeng X, Duan Y, Yang Z, Ma Y, Yang H, et al. Molecular mechanism of ensitrelvir inhibiting SARS-CoV-2 main protease and its variants. *Commun Biol* 2023;**6**:694.
28. Dampalla CS, Rathnayake AD, Perera KD, Jesri AM, Nguyen HN, Miller MJ, et al. Structure-guided design of potent inhibitors of SARS-CoV-2 3CL protease: structural, biochemical, and cell-based studies. *J Med Chem* 2021;**64**:17846−65.
29. Sacco MD, Ma C, Lagarias P, Gao A, Townsend JA, Meng X, et al. Structure and inhibition of the SARS-CoV-2 main protease reveal strategy for developing dual inhibitors against M^{pro} and cathepsin L. *Sci Adv* 2020;**50**:eabe0751.
30. Xiao T, Cui M, Zheng C, Wang M, Sun R, Gao D, et al. Myricetin inhibits SARS-CoV-2 viral replication by targeting M^{pro} and ameliorates pulmonary inflammation. *Front Pharmacol* 2021;**12**:669642.
31. Palmier MO, Van Doren SR. Rapid determination of enzyme kinetics from fluorescence: overcoming the inner filter effect. *Anal Biochem* 2007;**371**:43−51.
32. Chen Y, Fu Z, Yan G, Lin Y, Liu X. Optimization of expression conditions and determination of the proteolytic activity of codon-optimized SARS-CoV-2 main protease in *Escherichia coli*. *Sheng Wu Gong Cheng Xue Bao* 2021;**37**:1334−45.
33. Rong Y, Zhang C, Gao WC, Zhao C. Optimization of the expression of the main protease from SARS-CoV-2. *Protein Expr Purif* 2023;**203**:106208.
34. Yang KS, Ma XR, Ma Y, Alugubelli YR, Scott DA, Vatansever EC, et al. A quick route to multiple highly potent SARS-CoV-2 main protease inhibitors. *ChemMedChem* 2021;**16**:942−8.
35. Zhu W, Xu M, Chen CZ, Guo H, Shen M, Hu X, et al. Identification of SARS-CoV-2 3CL protease inhibitors by a quantitative high-throughput screening. *ACS Pharmacol Transl Sci* 2020;**3**:1008−16.
36. Ma C, Sacco MD, Hurst B, Townsend JA, Hu Y, Szeto T, et al. Boceprevir, GC-376, and calpain inhibitors II, XII inhibit SARS-CoV-2 viral replication by targeting the viral main protease. *Cell Res* 2020;**30**:678−92.
37. Brier L, Hassan H, Hanoulle X, Landry V, Moschidi D, Desmarets L, et al. Novel dithiocarbamates selectively inhibit 3CL protease of SARS-CoV-2 and other coronaviruses. *Eur J Med Chem* 2023;**250**:115186.
38. Tietjen I, Cassel J, Register ET, Zhou XY, Messick TE, Keeney F, et al. The natural stilbenoid (−)-hopeaphenol inhibits cellular entry of SARS-CoV-2 USA-WA1/2020, B.1.1.7, and B.1.351 variants. *Antimicrob Agents Chemother* 2021;**65**:e0077221.
39. Barnett A, Tsvetanov S, Gamage N, Martin JL, Duggleby RG, McManus ME. Active site mutations and substrate inhibition in human sulfotransferase 1A1 and 1A3. *J Biol Chem* 2004;**279**:18799−805.
40. Reed MC, Lieb A, Nijhout HF. The biological significance of substrate inhibition: a mechanism with diverse functions. *Bioessays* 2010;**32**:422−9.
41. Liu Y, Kati W, Chen CM, Tripathi R, Molla A, Kohlbrenner W. Use of a fluorescence plate reader for measuring kinetic parameters with inner filter effect correction. *Anal Biochem* 1999;**267**:331−5.
42. Könczöl Á, Dargó G. Brief overview of solubility methods: recent trends in equilibrium solubility measurement and predictive models. *Drug Discov Today Technol* 2018;**27**:3−10.

43. Raevsky OA, Grigorev VY, Polianczyk DE, Raevskaja OE, Dearden JC. Aqueous drug solubility: what do we measure, calculate and QSPR predict?. *Mini Rev Med Chem* 2019;**19**:362−72.
44. Kerns EH, Di L, Carter GT. *In vitro* solubility assays in drug discovery. *Curr Drug Metabol* 2008;**9**:879−85.
45. Konno S, Kobayashi K, Senda M, Funai Y, Seki Y, Tamai I, et al. 3CL protease inhibitors with an electrophilic arylketone moiety as anti-SARS-CoV-2 agents. *J Med Chem* 2022;**65**:2926−39.
46. Hou N, Shuai L, Zhang L, Xie X, Tang K, Zhu Y, et al. Development of highly potent noncovalent inhibitors of SARS-CoV-2 3CLpro. *ACS Cent Sci* 2023;**9**:217−27.
47. Gao S, Song L, Claff T, Woodson M, Sylvester K, Jing L, et al. Discovery and crystallographic studies of nonpeptidic piperazine derivatives as covalent SARS-CoV-2 main protease inhibitors. *J Med Chem* 2022;**65**:16902−17.
48. Hattori SI, Higashi-Kuwata N, Hayashi H, Allu SR, Raghavaiah J, Bulut H, et al. A small molecule compound with an indole moiety inhibits the main protease of SARS-CoV-2 and blocks virus replication. *Nat Commun* 2021;**12**:668.
49. Greasley SE, Noell S, Plotnikova O, Ferre RA, Liu W, Bolanos B, et al. Structural basis for the *in vitro* efficacy of nirmatrelvir against SARS-CoV-2 variants. *J Biol Chem* 2022;**298**:101972.